Binding Site Recognition and Docking Dynamics of a Single Electron Transport Protein: Cytochrome c_2 (Supplementary Information)

Abhishek Singharoy,[†] Angela M. Barragan,[†,‡,§] Sundarapandian Thangapandian,[†,§] Emad Tajkhorshid,[†,¶] and Klaus Schulten[*,†,‡]

Beckman Institute for Advanced Science and Technology, University of Illinois at Urbana–Champaign, 405 N. Mathews Ave., Urbana, IL 61801, USA, Department of Physics, University of Illinois at Urbana–Champaign, 1110 W. Green St., Urbana, IL 61801, USA, and Department of Biochemistry, University of Illinois Urbana–Champaign, 600 S. Mathews Ave., Urbana, IL 61801, USA

E-mail: kschulte@ks.uiuc.edu

---

[*]To whom correspondence should be addressed
[†]University of Illinois at Urbana–Champaign, Beckman Institute
[‡]University of Illinois at Urbana–Champaign, Department of Physics
[¶]University of Illinois at Urbana–Champaign, Department of Biochemistry
[§]Contributed equally to this work

Table S1: In the left column, conventional names of the simulations, refering to the redox states of the cyt. c_1 and cyt. c_2 heme groups, are defined. The full number of simulated atoms, including protein, cofactors, water, lipids and ions, is listed for the performed MD and SMD simulations, together with system size and simulation time.

Simulated system	Atoms	System size (Å x Å x Å)	Simulation time (ns)	
			MD	SMD
$c_2^O c_1^R$	452,157	150 x 150 x 150	150	5 x 50
$c_2^O c_1^O$	452,157	150 x 150 x 150	150	
$c_2^R c_1^R$	452,157	150 x 150 x 150	150	
$c_2^R c_1^O$	452,157	150 x 150 x 150	150	5 x 50
c_1^R	86,596	60 x 60 x 60	150	
c_2^R	86,596	60 x 60 x 60	150	

Table S2: Docking energies of the most stable five cyt. c_2 - bc_1 complexes obtained from the DOT 2.0 protocol[1] . Atomic contact energy (ACE[2]), as well as Ruben Abagyan lab's atomic solvation potential (RAASP[3]) values are provided in units of kcal/mol.

Rank	ACE6	E_{elec}+ ACE6	RAASP1.4	E_{elec}+ RAASP1.4
1	-23.1667	-24.5703	-20.3029	-21.7065
2	-9.4630	-19.4735	-6.8745	-16.8850
3	-12.0590	-23.0085	-5.8048	-16.7543
4	-11.6154	-21.5715	-5.8637	-15.8198
5	-9.3411	-18.8181	-3.8153	-13.2923

Table S3: Long-range (charged-charged), mid-range (charged-polar, charged-nonpolar, polar-polar) and short-range (polar-nonpolar, nonpolar-nonpolar) inter-residue interaction energies and inter-center-of-mass distances of key interacting residues at the docked cyt. c_2 - bc_1 complex interface. The energies for four redox states are computed employing a modified generalized Born (GB) model.[4] Overall charge-charge interactions vary the most between the four different redox states, clearly showing a decrease in the interaction energy as one moves across the columns for a given row, i.e., from $c_2^O c_1^R$ to $c_2^R c_1^O$. The differences between redox states diminish with the interactions of less polar residues, and is minimal for hydrophobic contacts.

Type	cyt. c_2	cyt. c_1	Interaction Energy (kcal/mol)				Distance (Å)			
			$c_2^O c_1^R$	$c_2^O c_1^O$	$c_2^R c_1^R$	$c_2^R c_1^O$	$c_2^O c_1^R$	$c_2^O c_1^O$	$c_2^R c_1^R$	$c_2^R c_1^O$
Long-range	R32	E141	-27.03±4.34	-20.03±4.14	-9.10±3.62	-5.26±2.16	6.94±2.45	7.47±3.23	12.35±3.59	12.35±4.16
	R32	E147	-1.47±0.52	-0.53±0.11	0.00±0.03	0.00±0.14	15.29±2.12	15.29±3.20	17.35±4.04	16.76±4.20
	K35	E150	-11.42±3.12	-16.12±4.92	-13.22±4.12	-10.07±3.31	7.74±1.82	5.68±1.43	7.47±2.01	7.60±2.01
	K35	D152	-18.36±3.68	-0.69±0.29	0.00±0.2	-1.2±0.54	6.37±1.21	12.94±2.03	12.33±2.43	11.81±2.16
	K55	D152	-7.70±2.15	-5.08±2.05	-4.21±2.32	-4.05±2.72	8.97±2.51	9.74±2.38	9.94±2.35	9.94±3.01
	K95	D80	-21.88±4.92	-14.57±3.38	-6.54±3.38	-4.73±2.98	6.55±2.75	7.75±2.25	9.05±2.35	10.10±2.55
	K97	E95	-20.68±3.47	-7.25±3.18	-5.16±2.58	-3.50±2.45	7.25±2.02	8.74±2.51	9.64±2.78	11.80±2.75
	K99	E95	-8.25±2.27	-5.62±2.54	-4.97±2.98	-3.12±2.41	8.02±2.01	9.24±2.62	10.31±3.01	11.95±3.07
	K103	E34	-16.60±3.76	-13.35±3.24	-10.58±3.92	-11.95±4.02	6.94±2.17	7.34±2.59	8.04±1.85	7.64±2.89
	K105	E34	-20.49±4.99	-14.74±4.36	-11.23±4.68	-9.82±4.12	6.88±1.29	6.96±1.98	6.72±2.35	6.39±2.35
Mid-range	Q14	D191	-4.17±1.68	-3.06±1.42	-2.37±1.02	-2.24±1.13	7.66±1.62	7.50±1.71	7.82±1.45	7.2±2.15
	Q14	D192	-2.30±0.92	-2.55±1.09	-1.74±0.74	-1.58±0.72	9.86±1.62	9.46±1.55	10.24±1.98	10.54±1.77
	R32	P142	-1.50±0.17	-1.27±0.12	-0.62±0.31	0.00±0.14	12.86±3.02	12.06±2.15	14.64±4.02	13.88±4.11
	K35	P151	-1.69±0.50	-0.19±0.31	0.00±0.01	-0.86±0.21	9.60±1.26	9.94±1.82	9.13±2.52	8.82±1.42
	T36	Y155	-2.45±0.63	-1.76±0.35	-0.73±0.48	-1.2±0.53	6.96±1.38	6.76±1.25	7.64±1.33	6.96±1.02
	F54	D152	-1.42±0.32	-0.56±0.45	-0.81±0.42	-0.53±0.34	8.45±1.40	7.76±1.10	7.58±1.52	7.94±1.51
	K97	A93	-1.75±0.42	-1.14±0.50	-1.09±0.38	-0.45±0.31	6.47±1.23	6.05±1.25	6.60±1.69	6.88±1.92
	T101	C39	-2.26±0.35	-1.22±0.28	-1.32±0.58	-1.15±0.45	7.27±1.41	8.45±1.23	8.25±1.36	8.54±1.55
Short-range	Q14	M190	-2.88±0.32	-1.65±0.38	-1.31±0.32	-1.37±0.57	6.41±1.12	6.88±1.33	6.56±1.53	6.72±1.62
	T17	M190	-2.71±0.35	-2.28±0.65	-2.26±0.52	-2.05±0.72	6.49±1.83	6.64±1.42	6.49±1.37	6.51±1.02
	T101	A38	-3.85±0.67	-3.09±0.78	-3.69±0.75	-2.39±1.10	6.97±0.51	7.35±0.89	7.27±0.95	7.91±1.07
	F102	M190	-1.56±0.23	-1.63±0.22	-1.61±0.28	-1.23±0.27	6.68±0.71	6.28±0.78	6.59±0.89	7.07±0.84
	F102	L193	-3.22±0.23	-3.45±0.57	-3.31±0.58	-3.04±0.56	5.94±0.82	5.86±0.72	6.56±0.84	6.56±0.89
Cation-π	K35	F154	-1.45±0.25	-1.65±0.21	-1.53±0.13	-1.43±0.36	3.49±1.22	3.59±0.92	4.42±1.18	3.81±1.27

Table S4: Inter-heme distances for redox states $c_2^O c_1^R$, $c_2^O c_1^O$, $c_2^R c_1^R$ and $c_2^R c_1^O$. CBC represents the distance between the C_β carbons from the vinyl groups of cyt. c_2 and cyt. c_1 hemes; the edge-to-edge distance is measured between the C3C cabons of the respective heme pyrrole rings.[5] The distances shown change slightly during the 150 ns MD simulations performed for each state. The results are consistent with the observed stability of the minimal core across the four states. Inter-heme distances from the cyt. c_2 - bc_1 complex for *Rba. sphaeroides* agree well with those for the cyt. c_2 - bc_1 complex from yeast.

		Distance (Å)				
cyt. c_2 heme	cyt. c_1 heme	$c_2^O c_1^R$	$c_2^O c_1^O$	$c_2^R c_1^R$	$c_2^R c_1^O$	Yeast
CBC	CBC	4.06±0.76	4.07±0.75	4.15±0.82	4.36±0.88	4.1
Edge-to-Edge	Edge-to-Edge	8.48±0.21	8.68±0.35	8.68±0.27	8.98±0.68	9.1
Fe	Fe	16.49±0.34	16.53±0.28	16.51±0.55	16.59±0.59	17.4
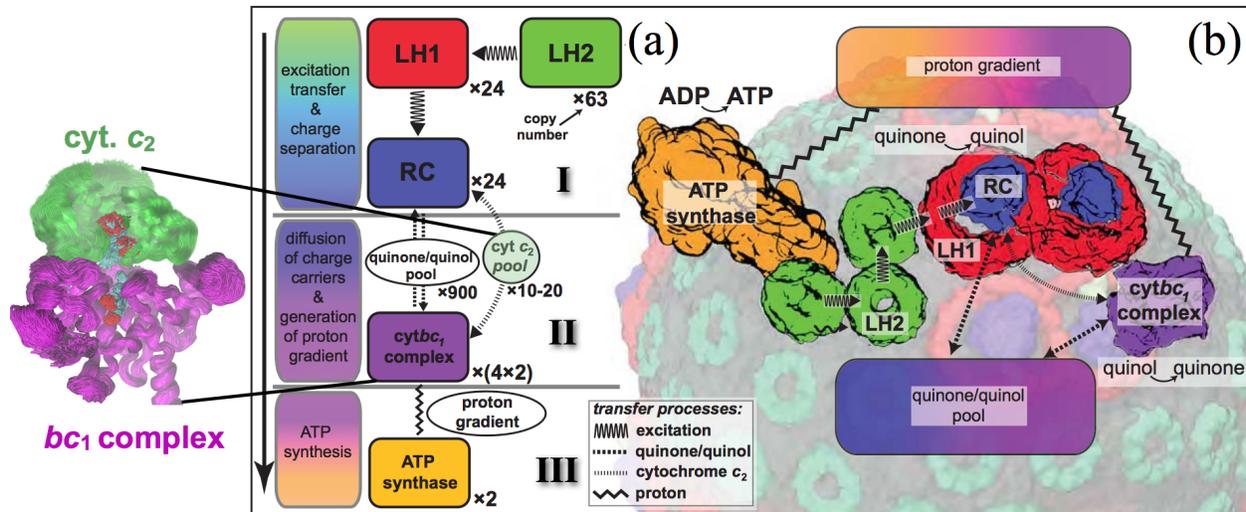
Figure S1: Processes involved in energy conversion in the photosynthetic chromatophore. **(a)** Energy conversion processes starting after initial light absorption are divided into three stages: I. Quinol production at RC as a result of excitation transfer. II. Diffusion between RC and bc_1 complex of quinone/quinol and cytochrome c_2, together with quinol-to-quinone conversion resulting in a proton gradient across the vesicle membrane. III. Utilization of proton gradient for ATP synthesis. **(b)** Chromatophore components, in which stages (1-3) take place, include LH2 (green), LH1 (red) - RC (blue), bc_1 complex (purple), and ATP synthase (brown) complexes as well as the lipid phase. (Inset) Docked cyt. c_2 ensemble (green) on the surface of the bc_1 complex (purple).
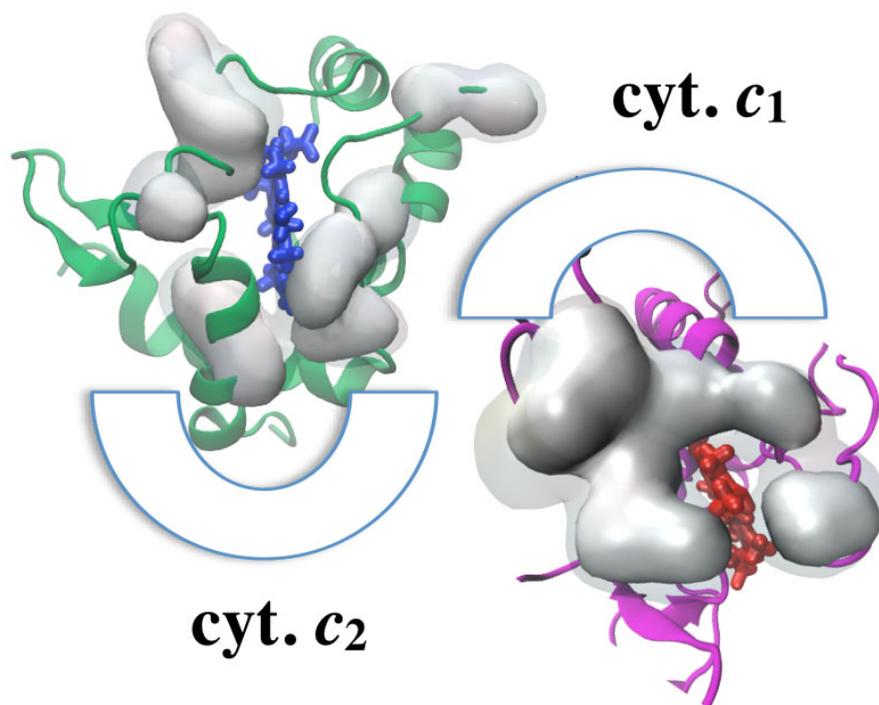
Figure S2: Hydrophobic residues at cyt. c_2 (left) and bc_1 complex (right). These residues are shown in surface representation at the binding interface demonstrating that their distribution changes negligibly between the post-ET (opaque representation) and the pre-ET (transparent) states.
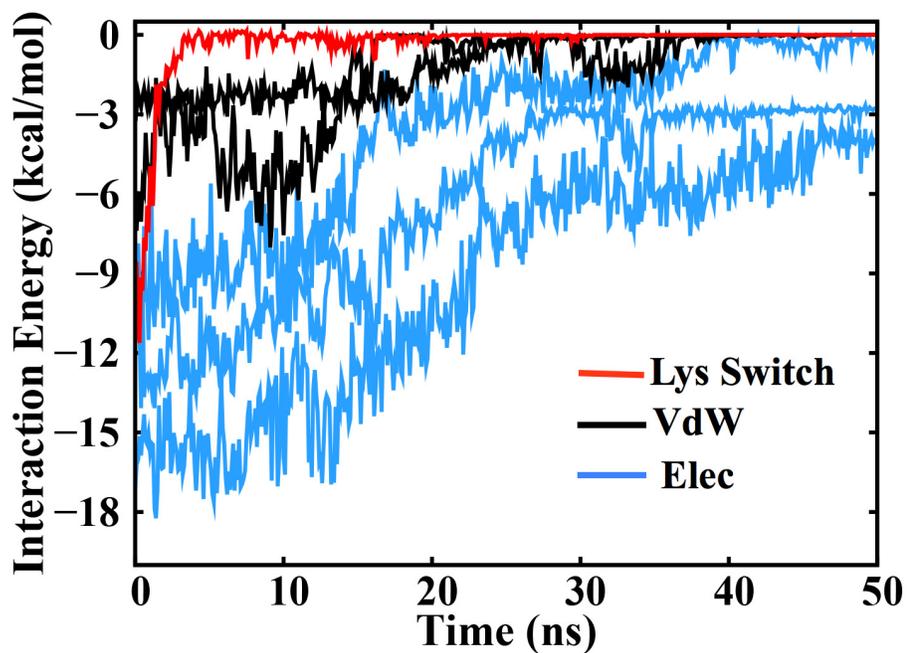
Figure S3: Inter-residue interaction energies showing that cyt. c_2 undocking is accompanied by breakage of the K99-E95 interaction (Lys switch), which generally precedes destabilization of the hydrophobic interactions (QT14-M190, 17-M190, T101-A38, F102-M190, F102-L193), the latter (vdW) ultimately followed by weakening of the water-mediated electrostatic (Elec) interactions (K32-E41, K35-E150, K35-D152, K103-E34, K105-E34).

(a)   (b)

electrostatic   **polar or hydrophobic**
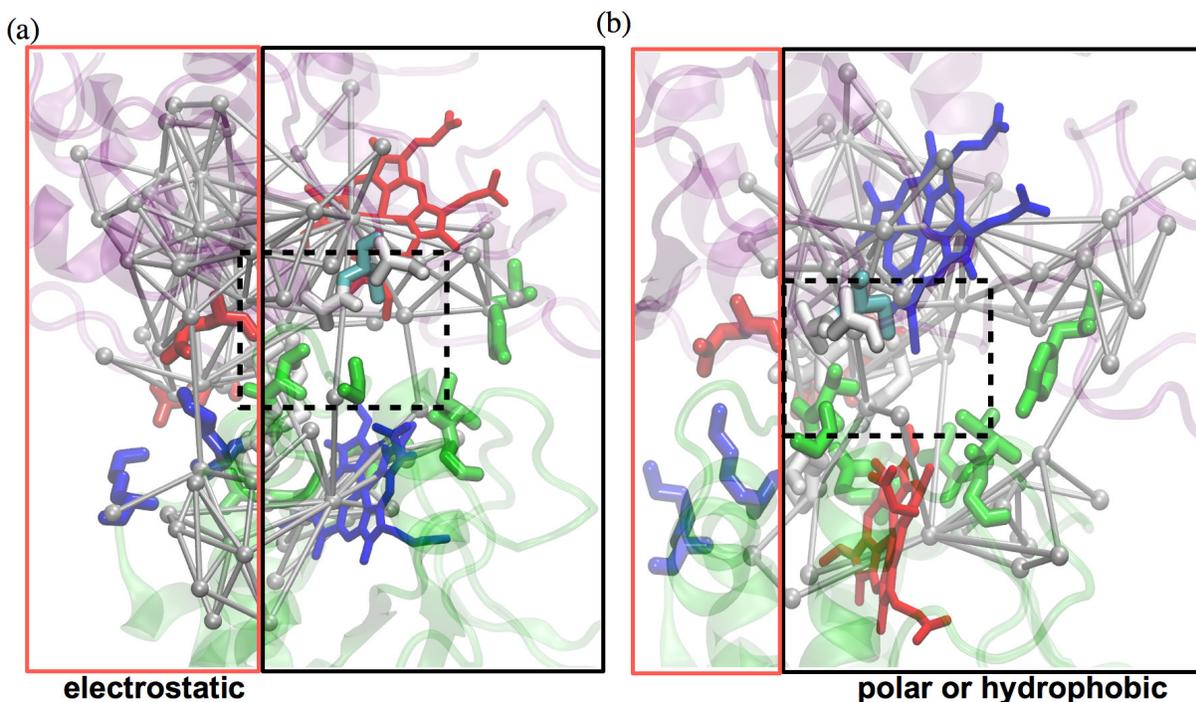
Figure S4: Dynamic correlation analysis of pre- and post-ET adhesion interactions between cyt. c_2 and bc_1 complex. The (electron) transfer links the redox states $c_2^O c_1^R$ and $c_2^R c_1^O$. The analysis is based on determining the correlation matrix $C_{ij} = \frac{\langle \Delta \vec{r}_i(t) \cdot \Delta \vec{r}_j(t) \rangle}{(\langle \Delta \vec{r}_i(t)^2 \rangle \langle \Delta \vec{r}_j(t)^2 \rangle)^{1/2}}$ of the docked cyt. c_2 - bc_1 complex system in states $c_2^O c_1^R$ and $c_2^R c_1^O$; i and j label the amino acids in the system. A so-called network analysis carried out within VMD employing the NetworkView plugin[6] determines key interaction routes in the system that are indicative of strong adhesive binding when residues of cyt. c_2 are connected with residues of the bc_1 complex. The residue centers are shown as (grey) spheres, connections as (grey) sticks. A red margin demarcates the part of the interface that contributes to electrostatic interactions; residues within the black margin are polar or hydrophobic, and the dotted box shows minimal core residues. **(a)** Correlation pathways in the state $c_2^O c_1^R$. The correlation pathways show that the positive residues (blue) from cyt. c_2 are dynamically correlated to the negative residues (red) from bc_1 complex; strong correlation is also seen between the polar and hydrophobic residues. **(b)** After electron transfer correlation between the charged residues (within the red margin) are lost indicating reduced electrostatic interactions between these residues; however, polar or hydrophobic residues (within the black margin) remain correlated contributing to interface stability.
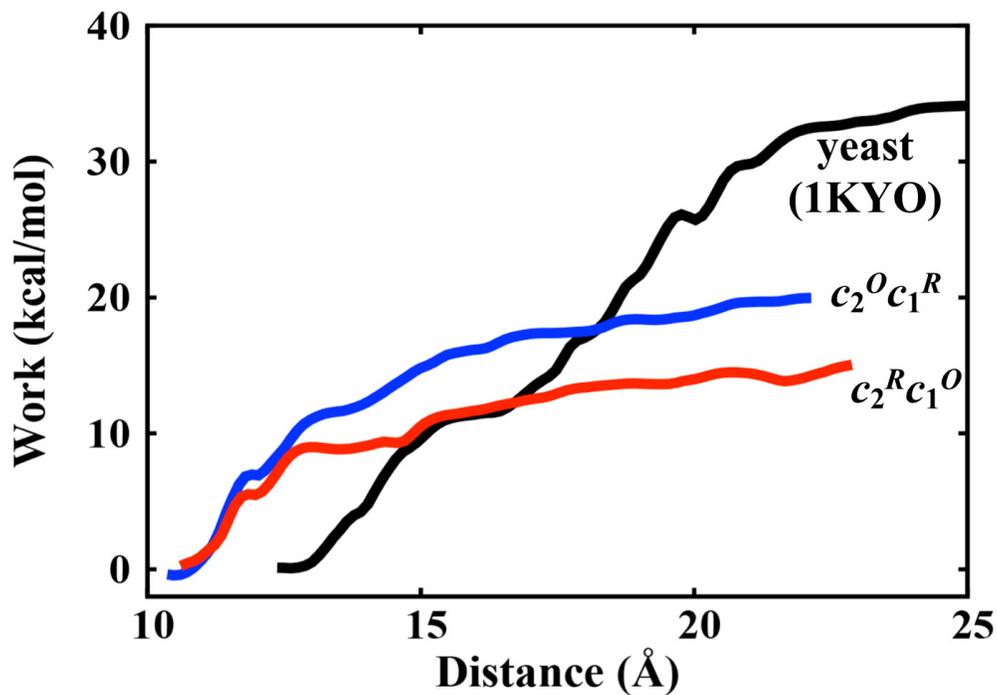
Figure S5: Nonequilibrium work as a function of cyt. c/c_2 displacement in yeast and in *Rba. sphaeroides* derived from SMD simulations. The work for unbinding yeast cyt. c (black) is greater than that of cyt. c_2 in $c_2^R c_1^O$ (red) and $c_2^O c_1^R$ (blue).
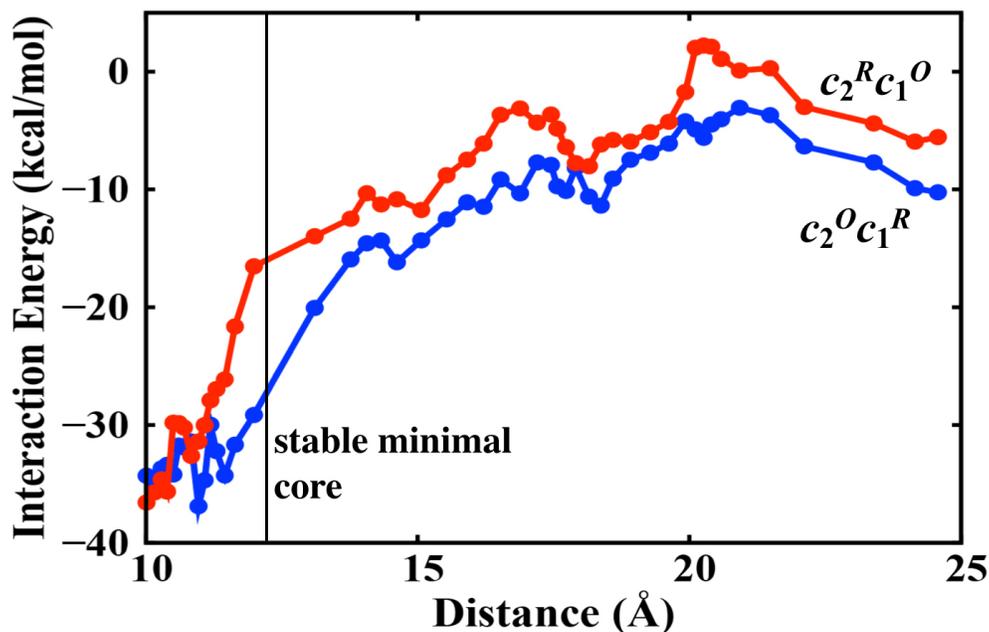
Figure S6: The van der Waals interaction energies, plotted against inter-heme edge-to-edge distance, show small changes when the distance increases from 10 Å to 12 Å (indicated by vertical line) during SMD, confirming stability of the minimal core during the first 2 Å of interface separation; inter-heme separation beyond 12 Å reduces the interaction energy, disrupting the hydrophobic interactions. The minimal core contacts in $c_2^R c_1^O$ (red) exhibit higher energy and, therefore, lower stability than those in $c_2^O c_1^R$ (blue).
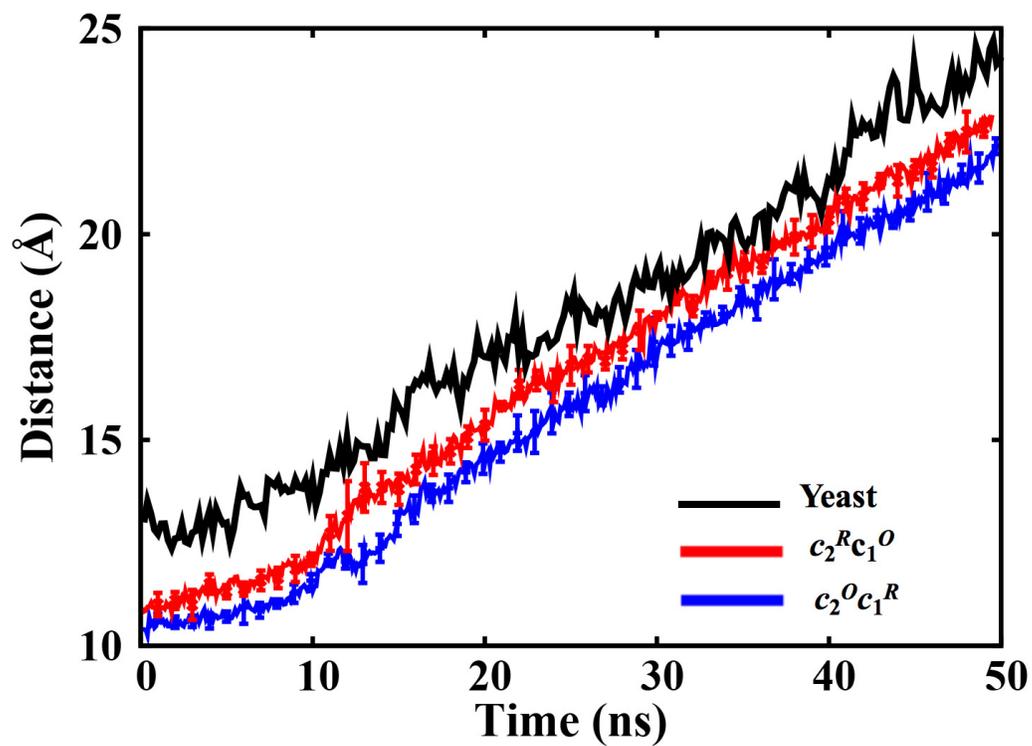
Figure S7: Distance between the heme of cyt. c/c_2 and the heme of cyt. c_1 during SMD simulations pulling cyt. c_2 and bc_1 complex apart. The distances plotted as a function of time are averaged over five SMD trajectories, showing that the distance is larger in case of the yeast system and smaller in case of the *Rba. sphaeroides* systems.
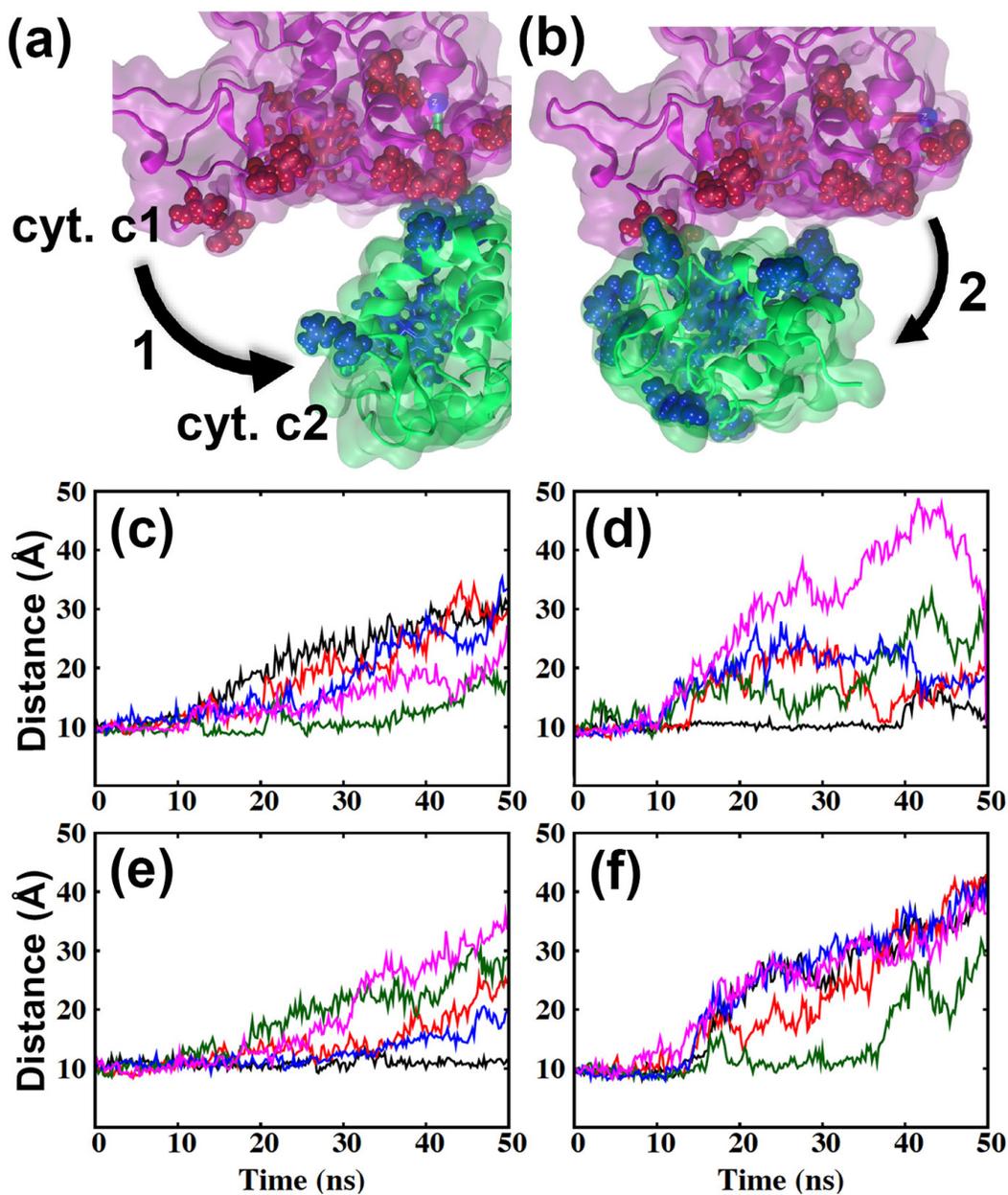
Figure S8: **(a,b)** Different modes of cyt. c_2 unbinding from the bc_1 complex induced by the same steering protocol. See also Fig. S6. Distance plots display the possible unbinding characteristics of $c_2^R c_1^O$ (c and d) and $c_2^O c_1^R$ (e and f). The initial unbinding can occur on either side of the interface. Center of mass distances between residue pairs P151 - F154 and A34 - G37 for Path-1 and between residue pairs T71 - D74 and G92 - K95 for Path-2 were used to quantify the observations. Results from five simulation copies are shown in black, red, green, blue, and magenta.
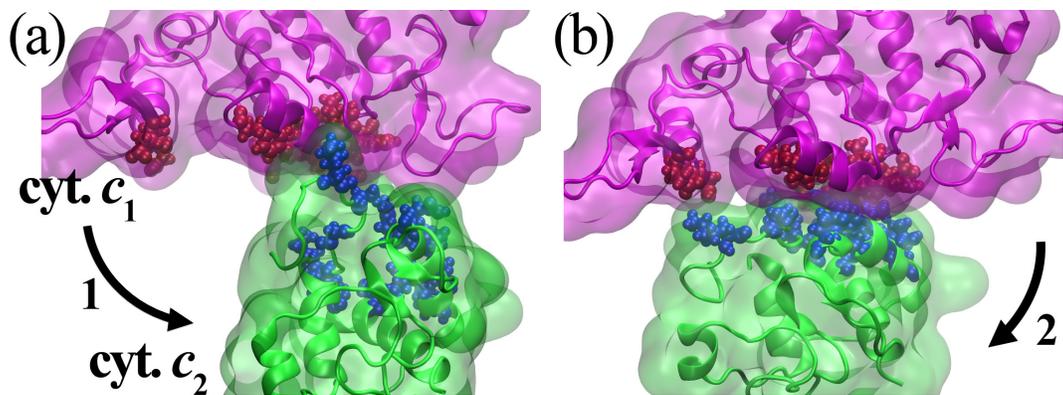
Figure S9: **(a,b)** Different modes of cyt. c unbinding from the bc_1 complex of yeast induced by the same steering protocol. The unbinding can occur from either sides of the interface converging to multiple weakly bound intermediate structures. Occurrence of these intermediates suggests the possibility of multiple equally-likely binding pathways, and that, binding begins with weak initial complexes which are subsequently transformed into an ensemble of stronger ones.
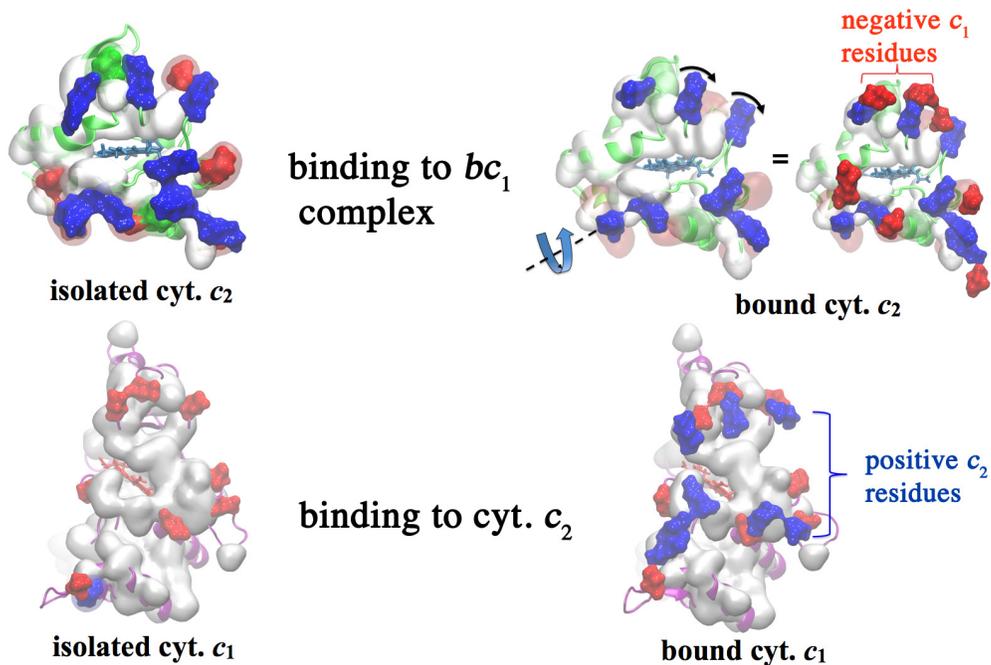
Figure S10: Mobility mismatch between cyt. c_2 and cyt. c_1 interfacial residues. (Upper left) Isolated cyt. c_2 binding-surface showing its electropositive residues (blue surfaces), intramolecularly coordinated to the negative or polar residues (red and green surfaces). (Upper center) Marginal separation of the bc_1 - bound cyt. c_2 protein with its positively charged residues displaced from the intra-cyt. c_2 salt bridges (transparent red and green surfaces). (Upper right) The displaced cyt. c_2 residues, in turn, form weaker and highly fluctuating, water mediated electrostatic interactions with complementary residues on the bc_1 complex surface (opaque red surface). (Lower left) Negatively charged residues on the surface of an isolated cyt. c_1 (red surface) are mostly uncoordinated. (Lower right) After cyt. c_2 binding, these residues are stabilized via coordination with the complementary positive residues of cyt. c_2.
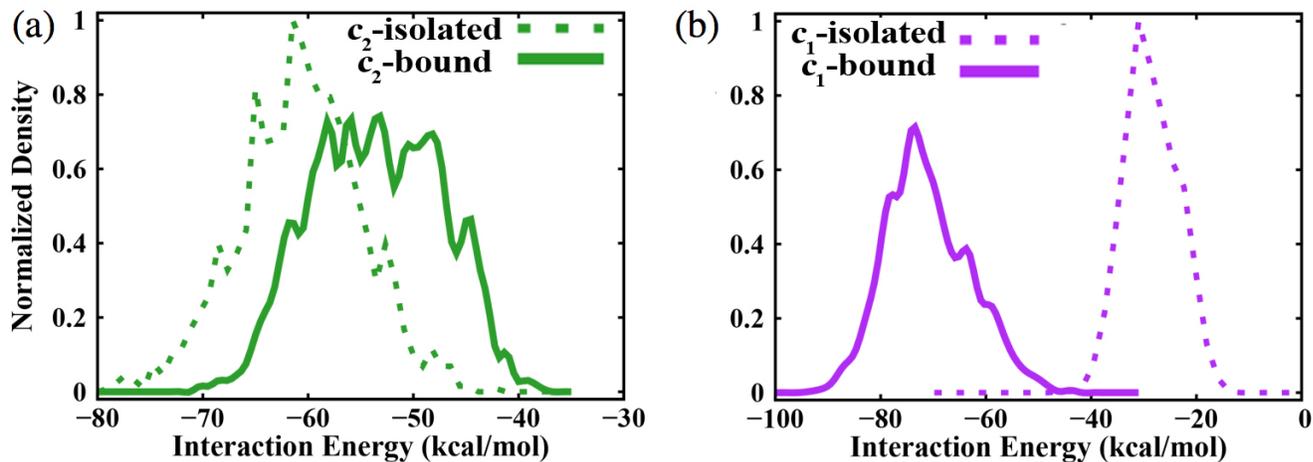
Figure S11: Distribution of binding surface intra- and intermolecular energies. **(a)** Energy distributions showing that the interfacial charged residues of cyt. c_2 become marginally destabilized on binding to bc_1 complex as intra-cyt. c_2 salt-bridge interactions are replaced by weaker water-mediated cyt. c_2 - cyt. c_1 electrostatic interactions. **(b)** The bc_1 complex residues are stabilized upon binding as they find complementary partners on the cyt. c_2 surface.
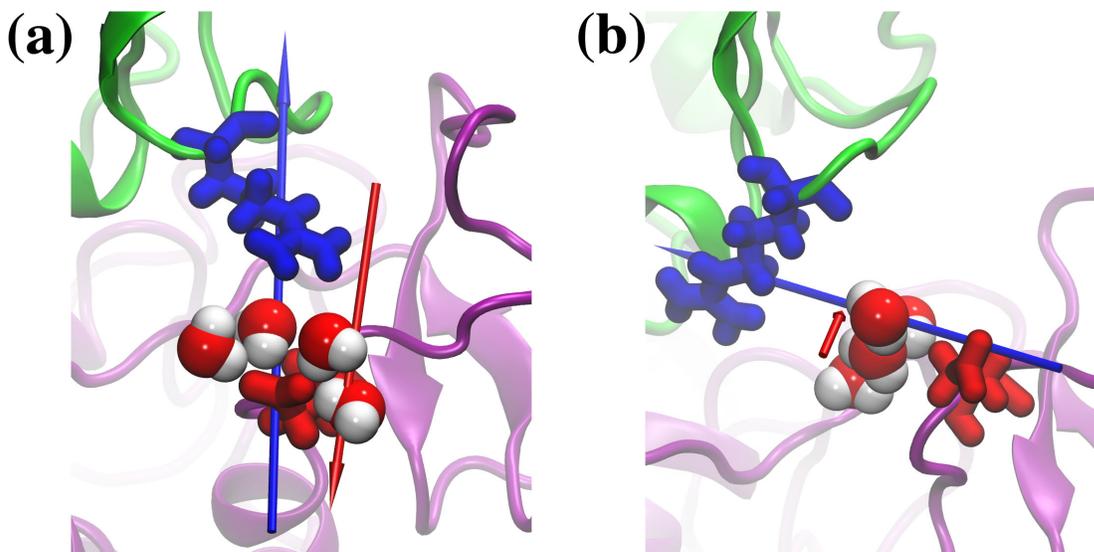
Figure S12: Water dipole order-to-disorder transition upon electron transfer. **(a)** In the $c_1^O c_2^R$ state, dipole moment (represented by the blue arrow) formed by a typical positively charged cyt. c_2 residue (R32) and a negatively charged cyt. c_1 residue (E141) orients the dipoles of the interfacial water molecules (red arrow) in the opposite direction, with the water-hydrogens pointing towards the bc_1 complex surface, thereby promoting hydrogen bond formation between water molecules and negatively charged bc_1 complex surface residues. **(b)** Electron transfer from cyt. c_1 to cyt. c_2 weakens interfacial electrostatic interactions, misaligns the inter-residue and interfacial water dipoles (pointing now in an orthogonal, rather than the opposite direction) and, therefore, orients the water molecules randomly (Fig. 4b inset and Fig. 3a).
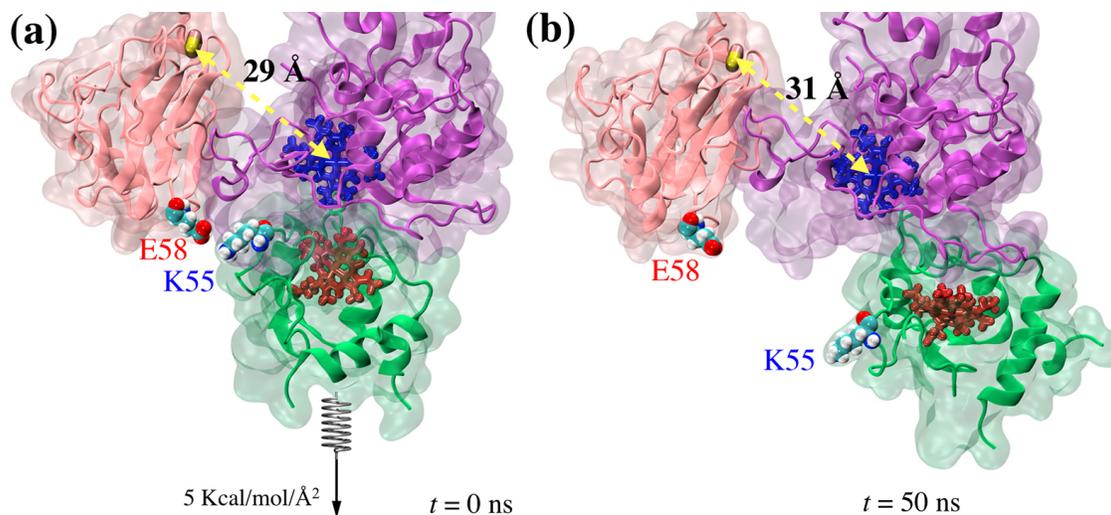
Figure S13: Steered molecular dynamics simulation pulling cyt. c_2 away from one of the cyt. c_1 subunits of the bc_1 complex. **(a)** System before pulling. Structure of cyt. c_2 (green, heme group dark brown), cyt. c_1 (purple, heme group dark blue) and the ISP (pink, iron-sulfur center Fe_2S_2 yellow) at t=0 and t=50 ns; spring indicating pulling location and direction is shown schematically; given is also the spring constant. **(b)** Structure of system after pulling. Shown are also the cyt. c_2 side group K55 and ISP side group E58. The initial salt bridge between the side group breaks apart during separation of cyt. c_2 from cyt. c_1, increasing the distance between Fe_2S_2 and cyt. c_1 heme.
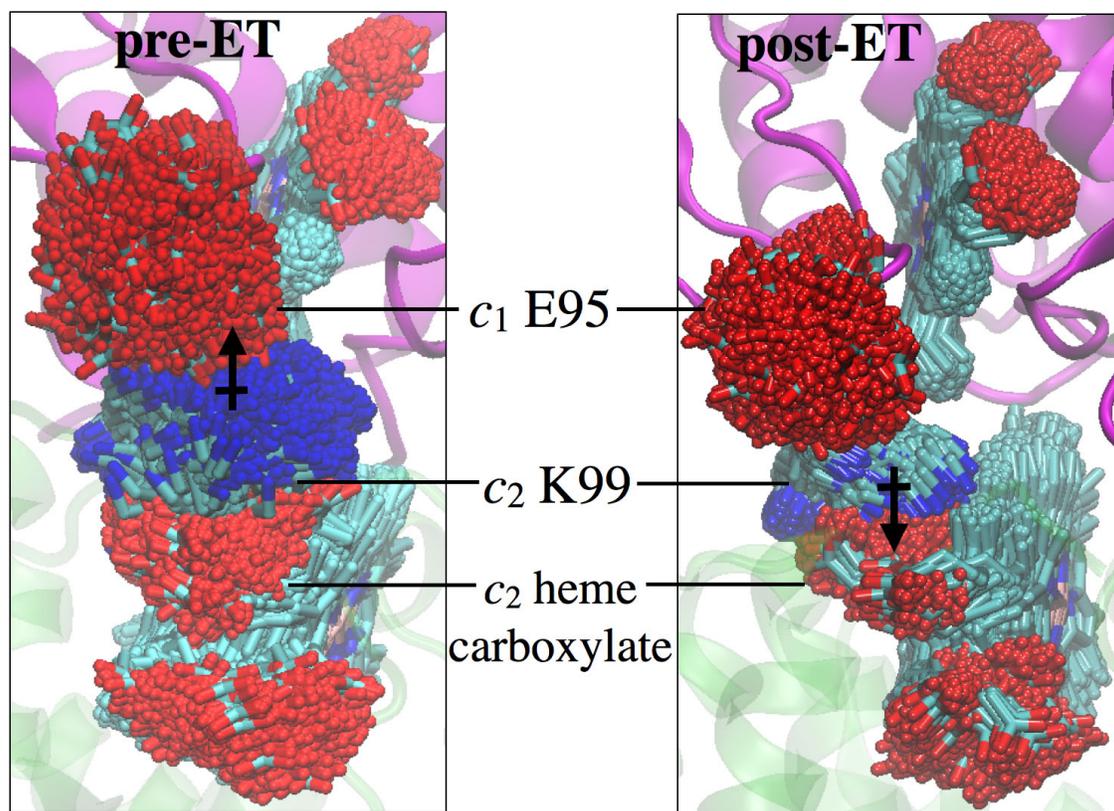
Figure S14: Ensemble view of the lyisne-switch before (pre-ET) and after (post-ET) electron transfer. The view demonstrates that a significant population of the K99 and E95 sidechains interact electrostatically in the pre-ET complex. This interaction is replaced by an interaction between K99 and heme carboxylates in the post-ET complex.

S1. Methods

Protein-protein docking

The docking program DOT 2.0[1] was employed to construct models of the cyt. c_2 - bound bc_1 complex. DOT uses convolution methods to perform a systematic rigid-body translational and rotational search. The van der Waals and electrostatic energies of both macromolecular components, cyt. c_2 and bc_1 complex, were mapped onto grids to compute explicit docking interactions. One of the two components was rotated and translated around the other to find the energetically most favorable conformations.

To guide the correct choice of docking protocols in DOT, first, a control study was performed for the determination of an already known complex; the cyt. c - bound bc_1 complex in yeast (PDB ID: 1KYO[7]) was chosen for this purpose. The cyt. c was extracted from the PDB structure and randomly reoriented before docking. Top 5 poses obtained from the docking calculation showed high structural similarity to the crystal structure. The best docked model showed an RMSD of 1.3 Å with respect to the crystal structure and an edge-to-edge distance of 4.8 Å which is near perfect given that the resolution of the crystal structure is 2.97 Å and the observed inter-heme distance is 4.5 Å. Consequently, the same protocol was employed for the docking of cyt. c_2 to the bc_1 complex of *Rba. sphaeroides*, as described in the following.

Within our docking protocol, the bc_1 complex was held stationary while cyt. c_2 was allowed to move. Atomic coordinates for *Rba. sphaeroides* cyt. c_2 and bc_1 complex were taken from PDB crystal structures PDBID: 1L9B[8] and PDBID: 2QJY,[9] respectively. A cubic grid of 192 Å extension in each direction with 1 Å spacing between points was used for the translational search. The rotational search included a set of 54,000 orientations sampled at a resolution of every 6°. Together, the ro-translation search resulted in $192^3 \times 54000 = 382$ billion configurations of cyt. c_2 relative to the bc_1 complex. The evaluation phase of DOT docking re-scored the top 2000 docked conformations using a sum of DOT electrostatic energy

and an empirical pairwise atomic contact energy (ACE)[2] with a 6 Å cutoff. Subsequently, the top 30 conformations were subjected to an additional re-scoring, based on the sum of DOT electrostatic energy and an exposed-area-based Ruben-Abagyan atomic solvation potential (RAASP)[3] term, with a 1.4 Å surface probe radius, to derive five putative models.

DOT 2.0 computed docking energies of the five putative cyt. c_2 - bc_1 complexes are in the range of -13.3 to -21.7 kcal/mol. The four top-scored models exhibit a clearly localized area of contact between cyt. c_2 and the cyt. c_1 subunit of the bc_1 complex (Fig. 1a), and have the cyt. c_2 and cyt. c_1 hemes in close proximity, with inter-heme distances ranging from 9.0 to 9.5 Å. Since the respective four structures displayed comparable inter-heme distances, the one with the most favorable interaction energy, namely -21.7 kcal/mol, was chosen as the optimally docked cyt. c_2 - bc_1 complex model to be investigated further.

Prior to the aforementioned docking protocol, protonation states of the cyt. c_2 protein and that of the bc_1 complex were determined at a pH of 7 employing the PROPKA software.[10] Protonation states of the transmembrane residues in bc_1 complex, in particular the charged ones, were further validated using CHARMM-GUI prior to MD simulations.

Modeling and molecular dynamics simulation

Fragments of antibody, used in crystallization, and Core I and II subunits of the bc_1 complex, were not included in the DOT 2.0 docking. The core subunits are not necessary for the bc_1 complex catalytic activity,[11] and are located on the opposite side of the membrane, at a distance beyond 60 Å from the cyt. c_2 - cyt. c_1 interface. The removal decreased the total number of atoms in the simulation by 100,000. Both quinone binding sites of the bc_1 complex, located respectively 35 Å and 60 Å away from the interface, and the Fe_2S_2 cluster of ISP were retained in the simulations. The Fe_2S_2 cluster parameters were adopted from Izrailev et al.[12,13] Topology and parameters for trimethylated lysine of cyt. c (M3Lys) were derived from lysine and tetramethylammonium (both present in CHARMM27[14,15]). Cyt. c - heme topology and parameters were taken from Autenrieth et al.[13,16] Cyt. b hemes and all

common residues were simulated with the standard CHARMM27 force field. Structures for MD simulations were generated with Membrane Builder [17–19] at the CHARMM-GUI website (http://www.charmm-gui.org). [20,21] The total system size with POPC membrane and all water molecules was 0.5 million atoms. Oxidation states of the heme groups were tuned to model four different redox states of the cyt. c_2 - bc_1 complex - $c_2^O c_1^R$, $c_2^O c_1^O$, $c_2^R c_1^R$, and $c_2^R c_1^O$ (superindices O and R imply oxidized and reduced states of the respective heme groups). Each of the four systems were simulated for 150 ns in membrane, after a 10 ns period of equilibration (Table S1). All MD simulations were performed with NAMD 2.11. [22] Also, two more 150 ns simulations were performed for isolated oxidized and reduced cyt. c_2 (c_2^O and c_2^R) in solution.

In the stated simulations, each of the four membrane systems was first subjected to 1000-5000 steps of conjugate gradient energy minimization. Then, all atoms, except those located in the lipid tails, were fixed and the system was brought to 310 K and equilibrated for 100 ps. Since the POPC bilayer provided by Membrane Builder in the CHARMM-GUI website (http://www.charmm-gui.org) is constructed with pre-equilibrated lipid molecules (each in 2000 different conformations, randomly selected from a 2.5 ns trajectory of a homogeneous lipid bilayer [17]), only a short equilibration period sufficed for relaxing the lipid tails. Subsequently, non-hydrogen atoms of the protein were restrained and the system was compacted for 150 ps at T = 310 K and P = 1 atm. Finally, all atoms were released from constraints and the four systems were equilibrated for 10 ns. The minimum distance between protein images resulting from the periodic boundary conditions was always higher than 15 Å. Langevin dynamics for all non-hydrogen atoms were carried out with a damping coefficient of 5 ps^{-1}. Simulations were performed with an integration time step of 1 fs where bonded interactions were computed every time step, short-range non-bonded interactions every two time steps, and long-range electrostatic interactions every four time steps. A cutoff of 16 Å was used for van der Waals and short-range electrostatic interactions: a switching function was started at 15 Å for van der Waals interactions to ensure a smooth cutoff.

A key interface property monitored during MD simulations was the contact area between binding surfaces of cyt. c_2 and cyt. c_1. The contact area was taken to be the difference between the sum of the solvent-accessible surface areas (SASA) of isolated cyt. c_2 and cyt. c_1, and the SAS of cyt. c_2 and cyt. c_1 taken together. SASA was calculated in VMD[6] using a probe radius of 1.4 Å.[13]

Dynamics of the interface residues were characterized employing positional variance computed by summing the deviation of individual atom positions and dividing the result by the number of atoms in the residue.[23] This measure is slightly different from the usual root mean square fluctuation (RMSF), which measures fluctuation from a fixed reference structure by aligning the structures, thus eliminating translational and rotational motions. In contrast, average positional variance calculated here contains contributions from overall displacements of the residues and their motions relative to the rotation/translation and internal motions of the assembly.

Computations of the electrostatic interaction energies presented in Tables 1 and S3 were performed employing the Generalized Born (GB) model[4] invoked through the NAMD energy plugin of VMD. Structures from the MD simulation, saved every 10 ps, were subjected to this computation for determining the instantaneous energies, which were then averaged over the entire ensemble. Since the MD simulated structures capture explicit solvation effects, the same reflect on the electrostatic interaction energies computed with the GB model. However, explicit charge-dipole interactions are missing between the protein and the solvent. These interactions are partially accounted for in GB through an implicit dielectric model.

Finally, distribution of interface water molecules was determined by applying the occupancy feature of VMD's volmap plugin.

Steered MD simulations

We performed a set of five steered MD (SMD) simulations, with the distance between center of masses of cyt. c_2 and cyt. c_1 set as a collective variable, to induce the undocking of cyt. c_2

from the bc_1 complex (listed in Table S1); note, only heavy atoms were chosen in computing the mass centers. SMD simulations were necessary, as the timescale of cyt. c_2 unbinding is beyond reach of equilibrium MD simulations. The simulations were repeated for the pre- and post-electron transfer states $c_2^O c_1^R$ and $c_2^R c_1^O$, respectively; altogether ten SMD simulations (five for each pre- and post-ET states) were performed, each for 50 ns with a 1 fs integration time step and a force constant of 5 kcal/mol/Å^2. During these simulations, forces were applied to increase by 12 Å the distance between the centers of masses of cyt. c_2 and bc_1 complex using a harmonic potential. A few short, 5-10 ns simulations were performed for different target distances; at 12 Å almost all interactions between the domains were lost. External forces were applied to all C$_\alpha$ atoms of cyt. c_2, of bc_1 complex residues 1 to 220 and to the heavy atoms of the heme groups. An identical protocol was used for both the pre- and post-ET states of the cyt. c_2 - bc_1 complex. Nonequilibrium work values were calculated for the SMD simulations to yield a measure of cyt. c_2 binding strength to bc_1 complex at different redox states. Pathways characterized by values of nonequillibrium work ranging between 10-30 kcal/mol are assumed to be biologically relevant.[24] The work performed by the harmonic force was computed by employing numerical integration of the force applied by the potential over time multiplied by the total displacement.[25] To summarize, the entire study involved a total simulation time of 150 ns × 6 for MD calculations and of 50 ns × 10 for SMD calculations, namely 1.4 μs.

S2. Cation-π interaction

All the four MD simulations summarized in Table S1 indicate cation-π interaction between residues K35 of cyt. c_2 and F154 of cyt. c_1. While cation-π interaction energies calculated from the cyt. c_2 - cyt. c_1 interfaces in simulations are in the range of -1.40 to -1.60 kcal/mol (Table 1c), they are significantly lower relative to energies derived from higher levels of theory, which are anywhere in the range of -2.90 to -7.76 kcal/mol.[13] Similar discrepancies have

been faced in the past; Hunte and co-workers have emphasized the importance of cation-π interactions in cyt. c docking to the bc_1 complex, whereas Paddock et al.[26] experimentally estimated the energy of a cation-π interaction at the interface between RC and cyt. c_2 to be only -0.6 kcal/mol. Furthermore, complexes of cytochrome c peroxidase with cyt. c (2PCB and 2PCC,[27] 2GB8[28]) do not exhibit any energetically favorable cation-π interactions, undermining any general role for cation-π interactions in cyt. c_2 docking to its binding partners. Also, available classical force fields are not adequate for computing cation-π interactions. Consequently, in MD simulations of the yeast cyt. c - bc_1 complex the cation-π interactions are replaced by salt bridges.[13] Thus, at this time it seems advisable to defer discussion of the role of cation-π interactions for docking cyt. c_2 to bc_1 complex until further quantitative experimental data are available. In any case a proper computational description of cation-π interactions requires a quantum chemical treatment.[5]

S3. Evolutionary conservation of interface residues

We note that some of the interface stabilizing residues on the bc_1 complex identified in the MD simulation of the pre-ET complex remain conserved in other life forms. While E141 remains conserved in *Rba. sphaeroides* (Rs), *Rba. capsulatus* (Rc), *Bos taurus* (Bt), *Saccharomyces cerevisiae* (Sc) and *Chlamydomonas reinhardtii* (Cr),[9] E34 remains conserved in Rs, Rc, Bt and Sc, D191 and D192 in Rs, Rc and Bt, and D152 in Rs and Rc. Similarly, cyt. c_2 residues R32, K97, K99, K103 and K105 are also found to be key in stabilizing the cyt. c_2 - RC interface of *Rba. sphaeroides*.[8,29–32] Such evolutionary evidence further supports the interaction analysis of Table 1 in demonstrating the essential role of interface-binding residues predicted from our docking analysis and MD simulations.

S4. Order-disorder transition of interface water

The interfacial water molecules transition from an ordered to a disordered state following electron transfer from cyt. c_2 to cyt. c_1 (Fig. 4b inset and Fig. 3a main text). The order-disorder transition in interfacial water can be explained at the molecular level as follows. Strong electrostatic interactions between the positively charged residues of cyt. c_2 and negatively charged residues of cyt. c_1 orient the interfacial water dipoles in a direction with the oxygen facing cyt. c_2 and hydrogen facing cyt. c_1 (Fig. S12a). This orientation promotes ordered, hydrogen-bonded, water on the bc_1 complex surface. In contrast, the interfacial electrostatic interactions are destabilized after the electron transfer from cyt. c_2 to cyt. c_1. As a result, dipoles between the negatively charged cyt. c_2 residues and positively charged cyt. c_1 residues, are disoriented, in turn, disturbing ordered orientation of the interfacial water. Subsequently the population of hydrogen-bonded water decreases, thus leading to the order-disorder transition.

S5. Non-equilibrium work profiles from SMD simulations of cyt. c_2 - bc_1 complex

Nonequilibrium work profiles derived from the SMD simulations, presented in Fig. S5, are consistent with the energy changes shown in Fig. 5, demonstrating that during the initial phases of unbinding most of the work is utilized in overcoming strong van der Waals and/or electrostatic interactions. For example, the work required to unbind cyt. c_2 from the $c_2^O c_1^R$ complex sharply grows to 10 kcal/mol over the first 15 ns of SMD, when most of the cyt. c_2 - cyt. c_1 interactions are overcome (Fig. 5), and plateaus out over the subsequent 35 ns. Also shown in Fig. S5, unbinding of cyt. c_2 from the $c_2^R c_1^O$ complex yields a very similar work profile. However, work required to separate the cyt. c_2 - cyt. c_1 interface is always greater for $c_2^O c_1^R$ than $c_2^R c_1^O$, confirming the former to be a stronger complex.

S6. Yeast cyt. c - bc_1 complex SMD

Given that several aspects of *Rba. sphaeroides* cyt. c_2 - bc_1 structure and dynamics under equilibrium conditions agree well with those of the cyt. c - bc_1 complex in yeast,[7,13,33] comparisons were extended to the nonequilibrium regime via SMD simulations. SMD simulation of the yeast cyt. c_2 - bc_1 complex (PDBID: 1KYO[7]) structure showed a nonequilibrium work profile very similar to that of the *Rba. sphaeroides* model (Figs. S5 and S6). Furthermore, similar to cyt. c_2, multiple cyt. c binding pathways are observed on the surface of the bc_1 complex (Fig. S9). The result is also consistent with NMR-driven rigid-body docking predictions on the feasibility of primary and secondary binding sites on the bc_1 complex surface to respectively promote strong and weak cyt. c binding;[34] our SMD results indeed converge to weakly bound states with almost one-thirds the interaction energy observed in the strongly bound equilibrium model.

However, the overall magnitude of nonequilibrium work to unbind cyt. c from the bc_1 complex in yeast is higher than the work needed to separate the complex in its $c_2^O c_1^R$ state in *Rba. sphaeroides*, which, in turn, is greater than the work needed to separate the complex in its $c_2^R c_1^O$ state, again in *Rba. sphaeroides*. Alternatively, for the same amount of work, separation of the cyt. c -bc_1 complex interface is lesser than that of the cyt. c_2 - bc_1 complex (Fig. S6). This result suggests that the yeast cyt. c - bc_1 complex has a stronger binding affinity than the *Rba. sphaeroides* cyt. c_2 - bc_1 complex. Greater binding affinity of the yeast complex, derived here, and larger area of contact computed from past MD simulations,[13] might explain also the more facile crystallization compared to the *Rba. sphaeroides* case. Nonetheless, agreement of cyt. c_2 half-ring binding pattern (Fig. 2), inter-heme distances (Table S4), interfacial solvent dynamics (Fig. 3a), minimal core conformations (Fig. 4c), and dynamics in the vicinity of the bc_1 complex (Figs. S8 and S9) with the docking of yeast analogues reinforce confidence in the docked model of the complex presented here.

S7. Structural transition of iron-sulfur protein

An additional observation is made on account of our simulations which is directly relevant to the mechanistic intricacies of cyt. c_2 unbinding. The SMD simulation that pulls away cyt. c_2 from the bc_1 complex affects also the cyt. c_1 - iron-sulfur protein (ISP) interface since the K55 residue of cyt. c_2 is involved in an electrostatic interaction with the E58 residue of the ISP (Fig. S13). As the K55 (cyt. c_2)-E58(ISP) interaction is wildly fluctuating, it is neither obvious from the docked models, nor is it found in any of the yeast crystal structures, and can only be recognized from the MD simulations. When the cyt. c_2 is pulled away from the bc_1 complex, the K55-D58 bond is disrupted between cyt. c_2 and the ISP, inducing a large-scale motion of ISP away from cyt. c_1 and towards the quinol binding site in the bc_1 complex.

The observed structural transition in the ISP is highly relevant to the overall mechanism of quinol oxidation at the bc_1 complex (outlined in Introduction), which relies on a bifurcated electron transfer from quinol:[35-37] a quinol from the quinone/quinol pool in the membrane docks to the bc_1 complex binding site. The first quinol electron is transferred to the ISP which is initially close to the quinol binding site. After this transfer, the ISP moves away from the binding site and towards cyt. c_1, transferring the electron to the cyt. c_1 heme group. In the meantime the second electron is transferred in a bifurcated fashion, from the quinol to heme b_L, located in the opposite direction of the first electron transfer route. The reason for this bifurcation is that the Q-cycle utilizes the second electron to reduce a quinone, such that the bc_1 complex maintains, for every two quinols oxidized to quinone, one quinone reduced to quinol, thereby conserving 50% of the energy. The bifurcation can be only achieved through perfect timing of the motion of the ISP towards the quinol binding site (to be in position to take the first electron) and its motion away from the binding site (then allowing the second electron to be transferred to heme b_L). Surprisingly, the timing of the ISP motion is controlled by the cyt. $c_1 \rightarrow$ cyt. c_2 transfer: just after this transfer, as our simulations show, the ISP is liberated from binding to cyt. c_1 and attracted towards the quinol binding site,

readying the proper electron transfer at the right moment.

References

(1) Roberts, V. A.; Thompson, E. E.; Pique, M. E.; Perez, M. S.; Ten Eyck, L. *J. Comp. Chem.* **2013**, *34*, 1743–1758.

(2) Zhang, C.; Vasmatzis, G.; Cornette, J. L.; DeLisi, C. *J. Mol. Biol.* **1997**, *267*, 707–726.

(3) Fernandez-Recio, J.; Totrov, M.; Skorodumov, C.; Abagyan, R. *Proteins: Struct., Func., Bioinf.* **2005**, *58*, 134–143.

(4) Tanner, D. E.; Chan, K.-Y.; Phillips, J. C.; Schulten, K. *J. Chem. Theor. Comp.* **2011**, *7*, 3635–3642.

(5) Trabuco, L. G.; Harrison, C. B.; Schreiner, E.; Schulten, K. *Structure* **2010**, *18*, 627–637.

(6) Humphrey, W.; Dalke, A.; Schulten, K. *J. Mol. Graphics* **1996**, *14*, 33–38.

(7) Lange, C.; Hunte, C. *Proc. Natl. Acad. Sci. USA* **2002**, *99*, 2800–2805.

(8) Axelrod, H. L.; Abresch, E. C.; Okamura, M. Y.; Yeh, A. P.; Rees, D. C.; Feher, G. *J. Mol. Biol.* **2002**, *319*, 501–515.

(9) Esser, L.; Elberry, M.; Zhou, F.; Yu, C.-A.; Yu, L.; Xia, D. *J. Biol. Chem.* **2008**, *283*, 2846–2857.

(10) Dolinsky, T. J.; Nielsen, J. E.; McCammon, J. A.; Baker, N. A. *Nucl. Acid. Res.* **2004**, *32*, W665–W667.

(11) Smith, P. M.; Fox, J. L.; Winge, D. R. *Biochim. Biophys. Acta – Bioener.* **2012**, *1817*, 872–882.

(12) Izrailev, S.; Crofts, A. R.; Berry, E. A.; Schulten, K. *Biophys. J.* **1999**, *77*, 1753–1768.

(13) Kokhan, O.; Wraight, C. A.; Tajkhorshid, E. *Biophys. J.* **2010**, *99*, 2647–2656.

(14) Brooks, B. R.; Bruccoleri, R. E.; Olafson, B. D.; States, D. J.; Swaminathan, S.; Karplus, M. *J. Comp. Chem.* **1983**, *4*, 187–217.

(15) MacKerell, A. D. et al. *J. Phys. Chem. B* **1998**, *102*, 3586–3616.

(16) Autenrieth, F.; Tajkhorshid, E.; Baudry, J.; Luthey-Schulten, Z. *J. Comp. Chem.* **2004**, *25*, 1613–1622.

(17) Jo, S.; Kim, T.; Im, W. *PLoS ONE* **2007**, *2*, e880.

(18) Jo, S.; Lim, J. B.; Klauda, J. B.; Im, W. *Biophys. J.* **2009**, *97*, 50–58.

(19) Wu, E. L.; Cheng, X.; Jo, S.; Rui, H.; Song, K. C.; Dávila-Contreras, E. M.; Qi, Y.; Lee, J.; Monje-Galvan, V.; Venable, R. M.; Klauda, J. B.; Im, W. *J. Comp. Chem.* **2014**, *35*, 1997–2004.

(20) Jo, S.; Kim, T.; Iyer, V. G.; Im, W. *J. Comp. Chem.* **2008**, *29*, 1859–1865.

(21) Brooks, B. R. et al. *J. Comp. Chem.* **2009**, *30*, 1545–1614.

(22) Phillips, J. C.; Braun, R.; Wang, W.; Gumbart, J.; Tajkhorshid, E.; Villa, E.; Chipot, C.; Skeel, R. D.; Kalé, L.; Schulten, K. *J. Comp. Chem.* **2005**, *26*, 1781–1802.

(23) Singharoy, A.; Polavarapu, A.; Joshi, H.; Baik, M.-H.; Ortoleva, P. *J. Am. Chem. Soc.* **2013**, *135*, 18458–18468.

(24) Moradi, M.; Tajkhorshid, E. *Proc. Natl. Acad. Sci. USA* **2013**, *110*, 18916–18921.

(25) St-Pierre, J.-F.; Bunker, A.; Róg, T.; Karttunen, M.; Mousseau, N. *J. Phys. Chem. B* **2012**, *116*, 2934–2942.

(26) Paddock, M. L.; Weber, K. H.; Chang, C.; Okamura, M. Y. *Biochemistry* **2005**, *44*, 9619–9625.

(27) Pelletier, H.; Kraut, J. *Science* **1992**, *258*, 1748–1755.

(28) Volkov, A. N.; Worrall, J. A. R.; Holtzmann, E.; Ubbink, M. *Proc. Natl. Acad. Sci. USA* **2006**, *103*, 18945–18950.

(29) Autenrieth, F.; Tajkhorshid, E.; Schulten, K.; Luthey-Schulten, Z. *J. Phys. Chem. B* **2004**, *108*, 20376–20387.

(30) Lancaster, C. R. D.; Michel, H. *Structure* **1997**, *5*, 1339–1359.

(31) Tetreault, M.; Rongey, S. H.; Feher, G.; Okamura, M. Y. *Biochemistry* **2001**, *40*, 8452–8462.

(32) Tetreault, M.; Cusanovich, M.; Meyer, T.; Axelrod, H.; Okamura, M. Y. *Biochemistry* **2002**, *41*, 5807–5815.

(33) Solmaz, S. R. N.; Hunte, C. *J. Biol. Chem.* **2008**, *283*, 17542–17549.

(34) Moreno-Beltrán, B.; Díaz-Quintana, A.; González-Arzola, K.; Velázquez-Campoy, A.; la Rosa, M. A. D.; Díaz-Moreno, I. *Biochim. Biophys. Acta – Bioener.* **2014**, *1837*, 1717 – 1729.

(35) Zhang, Z.; Huang, L.; Shulmeister, V. M.; Chi, Y.-I.; Kim, K. K.; Hung, L.-W.; Crofts, A. R.; Berry, E. A.; Kim, S.-H. *Nature* **1998**, *392*, 677–684.

(36) Hunter, C.; Daldal, F.; Thurnauer, M.; Beatty, J. *The purple phototrophic bacteria*; Springer Science & Business Media, 2008; Vol. 28.

(37) Cartron, M. L.; Olsen, J. D.; Sener, M.; Jackson, P. J.; Brindley, A. A.; Qian, P.; Dickman, M. J.; Leggett, G. J.; Schulten, K.; Hunter, C. N. *Biochim. Biophys. Acta – Bioener.* **2014**, *1837*, 1769–1780.